

First-Principles Molecular Dynamics Simulation and Conductivity Measurements of a Molten $x\text{Li}_2\text{O}-(1-x)\text{B}_2\text{O}_3$ System

Takahiro Ohkubo,^{*,†} Eiji Tsuchida,[‡] Mallory Gobet,^{§,||} Vincent Sarou-Kanian,^{§,||} Catherine Bessada,^{§,||} and Yasuhiko Iwadate[†]

[†]Graduate School of Engineering, Chiba University, 1-33 Yayoi-cho Inage-ku, Chiba 263-8522, Japan

[‡]National Institute of Advanced Industrial Science and Technology (AIST), Centeral-2, Umezono 1-1-1, Tsukuba 305-8578, Japan

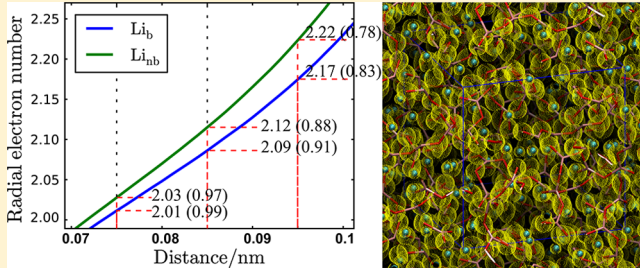
[§]CNRS, UPR3079, CEMHTI, 1D, avenue de la Recherche Scientifique, 45071 Orléans cedex 2, France

^{||}Faculté des sciences, Université d'Orléans, avenue du Parc-Floral, BP 6749, 45067 Orléans cedex 2, France



Web-Enhanced Feature

ABSTRACT: The electronic properties and atomic structure of a molten $x\text{Li}_2\text{O}-(1-x)\text{B}_2\text{O}_3$ system were investigated by measuring conductivity and using first-principles molecular dynamics (MD) simulations. The conductivities obtained were converted to a Li self-diffusion coefficient D_σ using the Nernst–Einstein equation to assess charge transfer mechanisms. D_σ was compared with a Li self-diffusion coefficient, D_{NMR} , which we measured in a previous study using high-temperature pulsed field gradient NMR. The D_{NMR}/D_σ of $x\text{Li}_2\text{O}-(1-x)\text{B}_2\text{O}_3$ ($0.2 \leq x \leq 0.5$) at 1250 K ranged from 2.5 to 3.2, following the same trend as room temperature ionic liquids. First-principles MD simulations were performed using our own finite element density functional theory code, FEMTECK (finite element method-based total energy calculation) for molten $x\text{Li}_2\text{O}-(1-x)\text{B}_2\text{O}_3$ systems at 1250 K. We found that the O–B–O angle distribution functions were characterized by a peak at approximately 120° . Although the electron number from the electronic radial distribution function was arbitrary with regard to the cutoff distance, the net Li charge calculated from the integrated electron number surrounding Li was approximately 0.9 at 0.085 nm. The mean square displacement (MSD) of Li as a function of time was evaluated from the atomic configuration. Li self-diffusion coefficients calculated from the MSD were in better agreement with experimental results than they were using classical MD.



INTRODUCTION

Studies in the field of electric devices have been performed to investigate structural aspects of ionic conducting materials and their correlation with electronic properties. Ionic conducting materials can be used as electrolytes in fuel cells and rechargeable batteries. The electrolyte in such electrochemical devices needs to be a simple buffer to allow internal ion flow between electrodes with high conductivity. Understanding mechanisms of ionic conduction and the related atomic structures is critical to the design of new electrolyte materials with optimum performance.

Boron oxide glasses designated as the $x\text{Li}_2\text{O}-(1-x)\text{B}_2\text{O}_3$ system are well-known stable solid-state materials that contain conducting Li^+ ions in a wide range of x values.^{1,2} The electrical conduction, density, and elastic properties of $x\text{Li}_2\text{O}-(1-x)\text{B}_2\text{O}_3$ glasses showed a nonlinear behavior when the Li_2O was increased. The discrepancy from linearity was called the borate anomaly. Because the glass network structure in these materials is key to ionic conduction, much research has involved structural modeling of the boron network using Raman^{3,4} and solid-state NMR^{5–8} spectroscopy. In addition, structural information on their melts at high temperature is required to

assess the properties of both melts and resulting glasses. One approach for understanding the local ion dynamic structure is applying computational techniques such as classical molecular dynamics (MD) simulations. The effects of the alkali content and temperature on the microstructure of lithium borate glasses have been investigated using classical MD simulation.^{9,10} Although the simulated Raman and infrared adsorption spectra in these studies have agreed with experimental observations, the potentials used in classical MD simulations have been based on *ad hoc* expressions by introducing three-body potential and a scaling factor for ionic charges.

A common complex feature of alkali borate glasses originates from various B–O bonds, in which the B atoms can have different hybridization states, sp^2 in BO_3 and sp^3 in BO_4 . Therefore, classical MD simulation gives only limited information about the glass network structure and electronic properties.

Received: December 18, 2012

Revised: April 10, 2013

Published: April 16, 2013

This study is a continuation of our previous study of Li transport in $x\text{Li}_2\text{O}-(1-x)\text{B}_2\text{O}_3$ melts provided by measuring electronic conductivity. The results obtained are compared with Li self-diffusion coefficients, measured using high-temperature pulsed field gradient NMR, to assess ionic transport. In addition, we present results of first-principles MD simulations of $x\text{Li}_2\text{O}-(1-x)\text{B}_2\text{O}_3$ at 1250 K. Applying first-principles MD simulation to a boron-oxide system is a suitable approach for understanding $x\text{Li}_2\text{O}-(1-x)\text{B}_2\text{O}_3$ melts, because all of the atomic and electronic properties are derived without using an arbitrary potential expression, such as the empirical model in the classical MD. Here we present results of first-principles MD simulation for investigating the detailed structural and electronic properties of $x\text{Li}_2\text{O}-(1-x)\text{B}_2\text{O}_3$ melts with $x = 0.1, 0.2, 0.3, 0.4, and 0.5 .$

EXPERIMENTAL SECTION

Conductivity. We prepared $x\text{Li}_2\text{O}-(1-x)\text{B}_2\text{O}_3$ glass samples for conductivity measurements in the same manner as in our previous study.¹¹ The polarization-free resistance of the melt was measured using an AC Wheatstone-type bridge with input frequencies from 0.5 to 10 kHz using Pt electrodes and an alumina vessel. A schematic diagram of the apparatus and the detailed experimental procedure have been reported.¹² The electrical conductivity was calculated from the real electrolytic impedance using the cell constant, which was calculated from measurements of known substances such as molten KNO_2 .¹³ The molar conductivities, σ , of $x\text{Li}_2\text{O}-(1-x)\text{B}_2\text{O}_3$ melts were derived from the system density.¹⁴

First-Principles MD Simulation. We conducted classical MD simulations using reported potential parameters⁹ without harmonic three-body interactions to obtain a suitable initial atomic configuration at the start of the first-principles MD simulations. The systems used for the calculations were composed of approximately 200 particles, including Li, B, and O atoms, with the desired compositions of $x\text{Li}_2\text{O}-(1-x)\text{B}_2\text{O}_3$ ($x = 0.1, 0.2, 0.3, 0.4, and 0.5). The initial configuration of each system was constructed by randomly introducing particles into the cell, the size of which was adjusted using the density derived from experimental results.¹⁴ Equations of motion were integrated using the Verlet algorithm with a time step of 1.0 fs, and the Ewald method was used to calculate electrostatic interactions. We carried out a thermal annealing procedure five times between 1250 and 6000 K.$

The first-principles MD simulation was performed for the following initial configuration, which was obtained from classical MD simulation. The electronic structures of the systems were evaluated using density functional theory in the Kohn–Sham formalism.¹⁵ We used a generalized gradient approximation in the Perdew–Burke–Ernzerhof (PBE) form, which was expected to give an accurate description. Adaptive finite elements were used instead of ordinary plane waves for the basis set.^{16,17} All production runs in the study were performed with an average cutoff energy of 75–85 Ry. In the MD part, the nuclei were classically treated, and their equations of motion were integrated using the Verlet algorithm with the forces calculated from the electronic structure. The temperature was controlled using a Berendsen thermostat¹⁸ with a target temperature of 1250 K. The MD time step was 1.2 fs in the production run. During the MD simulations, the electronic states were quenched to the Born–Oppenheimer surface at every time step with the limited-memory variant of the quasi-Newton method. The wave functions were extrapolated from

previous time steps. All of the calculations were carried out using our own finite element density functional theory (DFT) code *FEMTECK* (finite element method-based total energy calculation kit) for at least 150 ps. The above method has been successfully applied to a liquid molecular system.¹⁹

RESULTS AND DISCUSSION

Molar Conductivity. The measured conductivity was converted into molar conductivity using the density expected from an empirical equation for different compositions and temperatures.¹⁴ The molar conductivities of the $x\text{Li}_2\text{O}-(1-x)\text{B}_2\text{O}_3$ system increased with temperature, as shown in Figure 1. Because the $\ln(\sigma)$ versus $1/T$ plots for the investigated

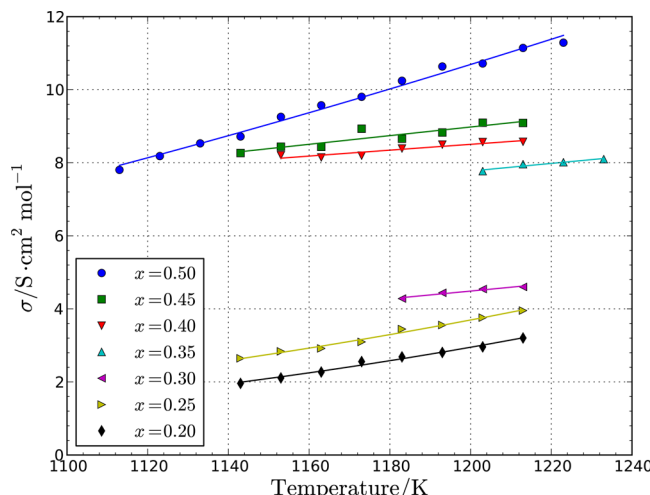


Figure 1. Variation of the molar conductivity σ with various temperatures in the molten $x\text{Li}_2\text{O}-(1-x)\text{B}_2\text{O}_3$ system. Solid lines indicate the expected values using the activation energy.

system were linear (data not shown), the molar conductivities were parametrized with the conventional Arrhenius-type equation

$$\sigma = A \exp\left(-\frac{E_a}{RT}\right) \quad (1)$$

where R is the gas constant, A is a constant, and E_a is the conductivity activation energy. The solid lines in Figure 1 indicate the expected values using E_a , calculated using Arrhenius-type fitting curves against temperature. The estimated E_a values are shown in Table 1.

Table 1. Activation Energy for Molar Conductivity of the Molten $x\text{Li}_2\text{O}-(1-x)\text{B}_2\text{O}_3$ System

x	0.20	0.25	0.30	0.35	0.40	0.45	0.50
E_a (kJ/mol)	78.4	67.6	28.2	16.1	11.2	15.7	38.1

In a previous paper, we reported high-temperature pulsed field gradient NMR diffusion measurements of ^{7}Li in $x\text{Li}_2\text{O}-(1-x)\text{B}_2\text{O}_3$ melts as a function of temperature and composition.¹¹ Self-diffusion measurements using NMR are fundamentally observations of the displacement of position-encoded spins during diffusion times on the order of milliseconds. Self-diffusion coefficients measured by NMR are very similar to the coefficients obtained using the conventional tracer diffusion method.²⁰ We compared the displacement

diffusion obtained from ^7Li NMR measurements and ionic conduction in the $x\text{Li}_2\text{O}-(1-x)\text{B}_2\text{O}_3$ melts by converting σ into charge diffusivity, D_σ using the Nernst–Einstein relationship

$$D_\sigma = \frac{RT\sigma}{q^2 F^2} \quad (2)$$

where F is the Faraday constant and q is the ionic charge. We calculated D_σ with a Li charge +1.0. The ratio between displacement and charge diffusivity has been called the Haven ratio,²¹ which contains information about the tracer and charge transport mechanisms. Figure 2 shows the D_{NMR} and D_σ values

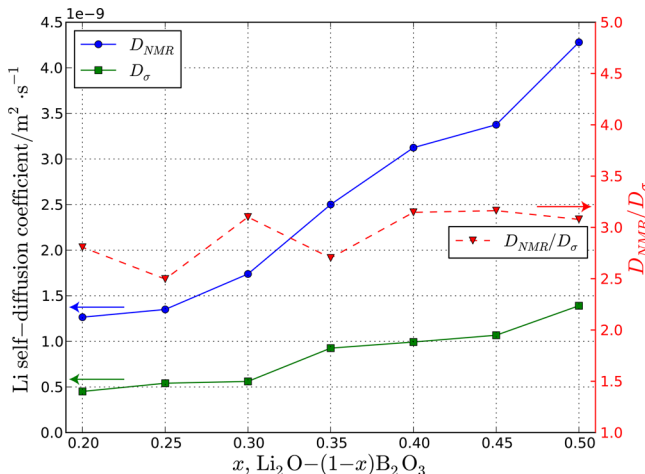


Figure 2. Left axis: comparison of ^7Li self-diffusion coefficients measured by NMR D_{NMR} ¹¹ and charge diffusivity D_σ obtained from the conductivity measurements as a function of composition at 1250 K. These values were estimated from the interpolation using activation energy obtained from the temperature-dependent data. Right axis: the D_{NMR}/D_σ ratio was plotted as a function of the composition.

at 1250 K on the left axis. These values were estimated by interpolating the temperature-dependent ^7Li self-diffusion coefficients and conductivity data from this study. The D_{NMR}/D_σ ratio is plotted on the right axis in Figure 2. It can be seen that the D_{NMR} values were larger than the D_σ values regardless of composition, and the D_{NMR}/D_σ values ranged from 2.5 to 3.2 for the compositions studied.

In contrast to our D_{NMR}/D_σ results, Haven ratios less than unity have been reported for all of the glasses. Thomas and Peterson measured the composition dependence of the Haven ratios for sodium germanate glasses, $x\text{Na}_2\text{O}-(1-x)\text{Ge}_2\text{O}_3$,²⁶ and found that the Haven ratios were close to 1.0 for low x values and decreased with increasing x . At $x = 0.3$, the Haven ratio was approximately 0.3. A similar general dependence of the Haven ratios on alkali oxide glass composition has been reported for sodium silicate glasses by several researchers.²³ It has been argued that diffusion coefficients based on ionic displacement were lower than expected from the ion's random path because of correlation effects between successive ionic jumps,²² but D_σ is not affected by these effects. The molar conductivity ratio, $\sigma/\sigma_{\text{NMR}}$, has been reported for ionic liquids at room temperature^{24,25} with the σ_{NMR} being calculated from self-diffusion coefficients measured by pulsed field gradient NMR using eq 1. The $\sigma/\sigma_{\text{NMR}}$ values for room-temperature ionic liquids were less than unity, indicating that the D_{NMR}/D_σ values were greater than unity. This was because of the

presence of noncharged species caused by strong interactions between the ions that do not contribute to conduction. However, these arguments for the obtained values of D_{NMR}/D_σ and $\sigma/\sigma_{\text{NMR}}$ are questionable. For further clarification of the relationship between D_{NMR} and D_σ , we will discuss the atomic and electronic structures on the basis of results of first-principles MD simulations.

First-Principles MD Simulation. A snapshot of the molten $0.4\text{Li}_2\text{O}-0.6\text{B}_2\text{O}_3$ system at 1250 K, using the visual molecular dynamics program,²⁶ is shown in Figure 3. Red and pink bars

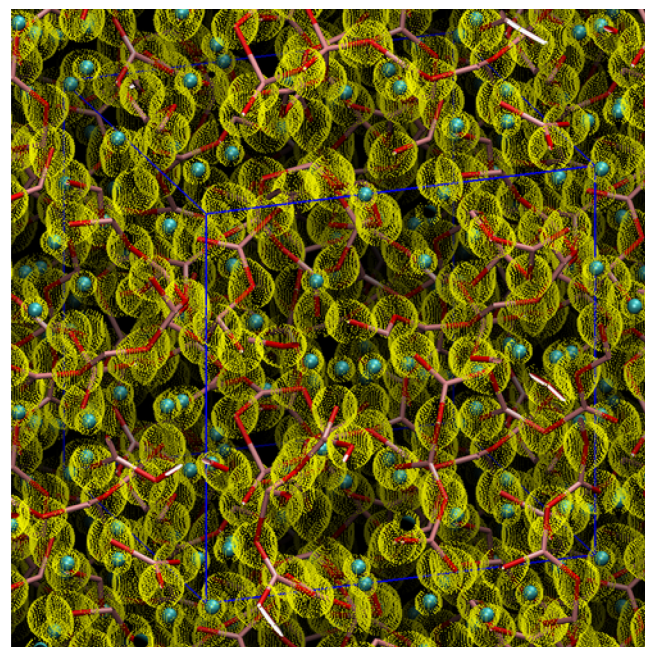


Figure 3. A snapshot of a molten $0.4\text{Li}_2\text{O}-0.6\text{B}_2\text{O}_3$ system at 1250 K. Red and pink bars indicate B and O, respectively, and cyan balls indicate Li. Yellow dots correspond to the electron density. Blue lines indicate the boundary of the calculated unit cell.

indicate B and O, respectively, and cyan balls denote Li. Yellow dots and blue lines indicate the electron density isosurfaces and the boundary of the calculated unit cell, respectively. The presence of sp^3 - or sp^2 -hybridized B was observed with the electron distribution around the B–O bonds. In addition, Li with a spherical electron distribution corresponding to 1s was located in the cavities of B and O glass networks. A video of Li moving back and forth within a cavity for a period of 1 ps is available as a web-enhanced object. A more quantitative assessment of the structure of the glass network containing Li can be conducted using other analyses.

The B–O pair radial distribution functions (PDFs) are shown in Figure 4. The first peaks are observed at 0.143 nm and ranged from 0.12 to 0.18 nm. Crystalline structures such as $\text{Li}_2\text{B}_4\text{O}_7$, $\text{Li}_3\text{B}_7\text{O}_{12}$, LiB_3O_5 , and Li_2O have been reported for Li–B oxide materials.^{27–29} The shortest distances between B and Li in these crystal systems were between 0.132 and 0.137 nm. Reverse Monte Carlo simulations of $\text{Li}_2\text{O}-2\text{B}_2\text{O}_3$ glass neutron diffraction showed that the first peak in the B–O PDF has two peak maxima at approximately 0.140 and 0.166 nm (values measured from an illustration in the paper).³⁰ The peak at 0.140 nm agrees well with our first-principles MD simulation in the molten state. However, the structural feature of the peak at 0.155 nm in the B–O PDFs disappeared in the melts.

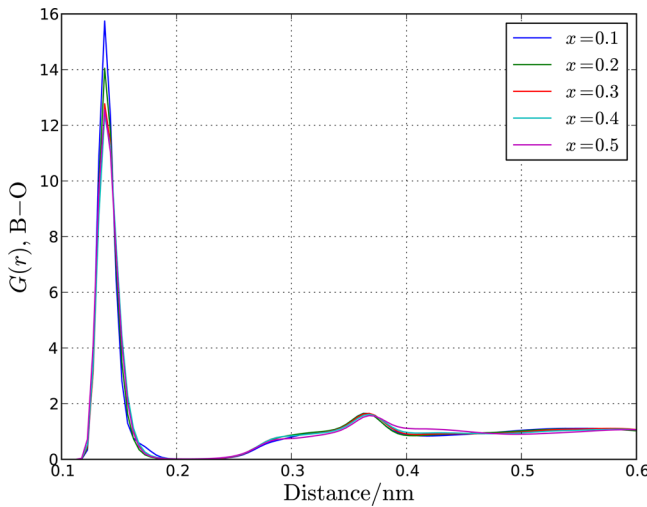


Figure 4. B–O pair radial distribution functions, $G(r)$, of a molten $x\text{Li}_2\text{O}-(1-x)\text{B}_2\text{O}_3$ system at 1250 K.

To determine the nature of the glass network with respect to B and O, the O–B–O angle distribution was examined from the atomic configurations. Figure 5 shows the O–B–O angles

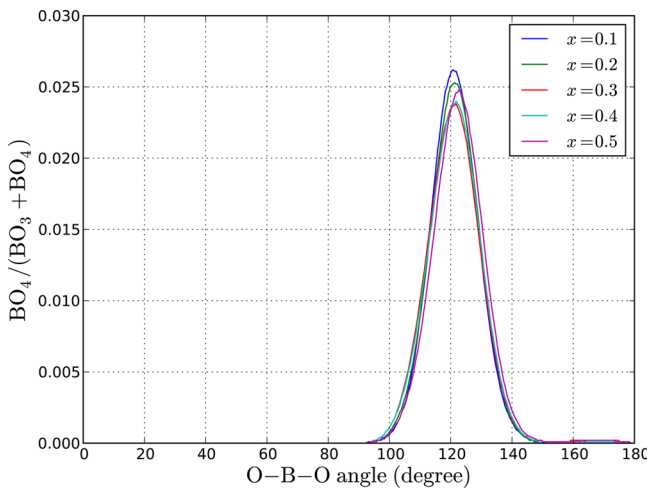


Figure 5. O–B–O bond angle distribution of a $x\text{Li}_2\text{O}-(1-x)\text{B}_2\text{O}_3$ system at 1250 K.

for the molten $x\text{Li}_2\text{O}-(1-x)\text{B}_2\text{O}_3$ system at 1250 K. The peaks were distributed around 120° regardless of the composition. We could assume that tetrahedral (BO_4^-) and trigonal planar B–O (BO_3) units could have been present, and these structures have O–B–O angles of 109.5 and 120° , respectively. Because two well-resolved peaks are not present, we believe that the B–O network structure is composed of strongly disordered BO_4^- and BO_3 units. Although the O–B–O angle distribution does not show distinctive peaks for BO_4^- and BO_3 units, BO_4^- unit molar fractions were examined from the atomic configuration on the basis of B–O distance.

We calculated the coordination number of O around B, within 0.18 nm, based on the B–O PDFs. All of the B can be classified as BO_3 or BO_4^- from the coordination number, and the $\text{BO}_4^-/(\text{BO}_3 + \text{BO}_4^-)$ values are displayed in Figure 6. The experimental curves for the $x\text{Li}_2\text{O}-(1-x)\text{B}_2\text{O}_3$ glasses, estimated from solid-state NMR at room temperature,³¹ are also plotted in Figure 6. The addition of alkali causes BO_3 to be

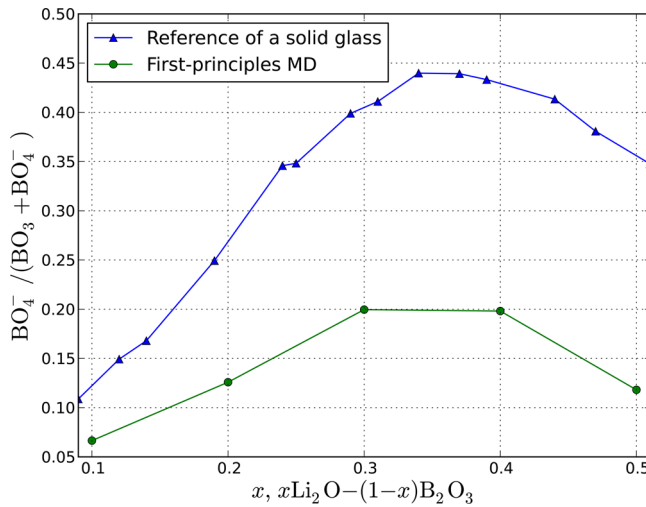


Figure 6. Mole fraction of BO_4^- units for $x\text{Li}_2\text{O}-(1-x)\text{B}_2\text{O}_3$ as a function of composition at 1250 K. Experimental results for the glasses at room temperature³¹ are included for comparison.

consumed in the transformation from BO_3 to BO_4^- . As a result, the $\text{BO}_4^-/(\text{BO}_3 + \text{BO}_4^-)$ values increase within the range $0 < x < 0.3$. For $x > 0.35$, there is an additional process of conversion of BO_3 and BO_4^- to BO_3^- and BO_3^{2-} , respectively, and $\text{BO}_4^-/(\text{BO}_3 + \text{BO}_4^-)$ values gradually decrease with increasing x .³² The $\text{BO}_4^-/(\text{BO}_3 + \text{BO}_4^-)$ trend with increasing x was well reproduced with our first-principles MD simulations; however, the calculated $\text{BO}_4^-/(\text{BO}_3 + \text{BO}_4^-)$ values were significantly lower than the experimental values at room temperature. This result is not particularly surprising given that the melting of the solid glass involves decreasing the amount of BO_4^- instead of increasing the amount of BO_3 , as a reported high-temperature Raman study of $x\text{Na}_2\text{O}-(1-x)\text{B}_2\text{O}_3$ melts.⁴ The decrement of half of $\text{BO}_4^-/(\text{BO}_3 + \text{BO}_4^-)$ values from the solid to the melt in the $x\text{Li}_2\text{O}-(1-x)\text{B}_2\text{O}_3$ system was in good agreement with experimental fact for the $x\text{Na}_2\text{O}-(1-x)\text{B}_2\text{O}_3$ system.

Li–O PDFs for the molten $x\text{Li}_2\text{O}-(1-x)\text{B}_2\text{O}_3$ system at 1250 K are shown in Figure 7. The mean Li–O distance corresponding to the first peak approximately ranged from 0.17 to 0.24 nm. These first peaks are slightly asymmetric and are

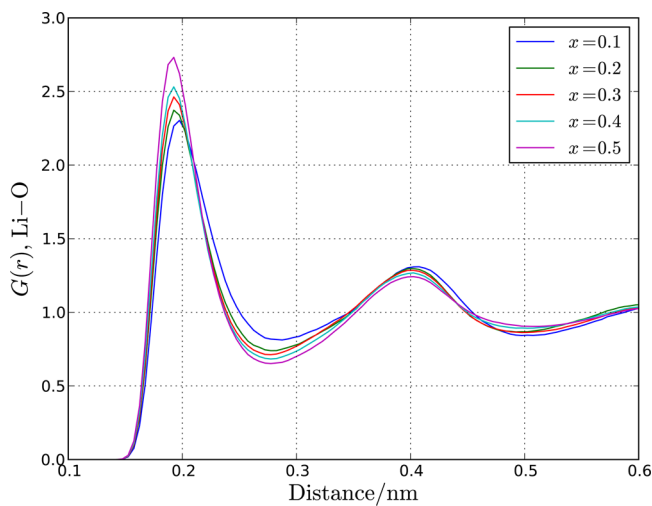


Figure 7. Li–O pair radial distribution functions $G(r)$ of a molten $x\text{Li}_2\text{O}-(1-x)\text{B}_2\text{O}_3$ system at 1250 K.

characterized by coordination numbers ranging from 3.95 to 4.24 within a cutoff distance of 0.27 nm. The Li structure in the LiBO_2 crystal systems was also studied using X-ray diffraction.³³ The Li–O distances in the LiBO_2 crystals were 0.1945, 0.1960, 0.1970, 0.2007, and 0.2473 nm.^{27–29,34} These local structures of Li–O pairs in the crystalline solids slightly varied in the melts. Two types of O are expected for the glass network form, where one is bridging oxygen atoms (O^{b}) bonding with two B and another is non-bridging oxygen atoms (O^{nb}) bonding with only one B within the coordination sphere. We identified O^{b} and O^{nb} from the boron coordination number around oxygen on the basis of the coordination sphere of the B–O bond cutoff distance of 0.18 nm. Having distinguished the O types, we present the Li– O^{b} and Li– O^{nb} pair distribution functions for the $x\text{Li}_2\text{O}-(1-x)\text{B}_2\text{O}_3$ molten system in Figure 8. Focusing

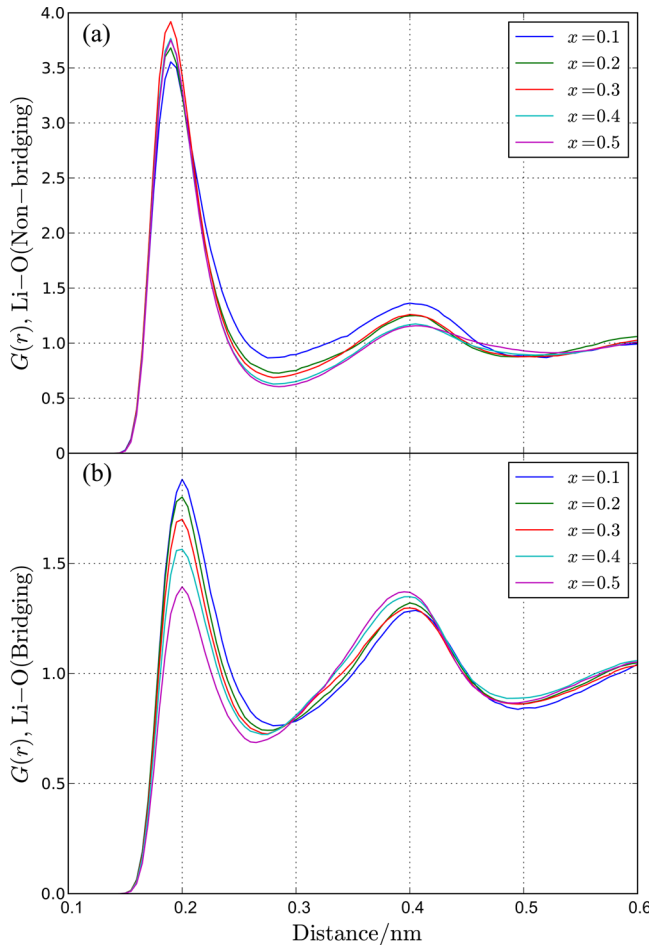


Figure 8. Li–O(bridging oxygen) and Li–O(non-bridging oxygen) pair radial distribution functions $G(r)$ of a molten $x\text{Li}_2\text{O}-(1-x)\text{B}_2\text{O}_3$ system at 1250 K.

on the first peak, the Li– O^{b} and Li– O^{nb} bonds have first peak maxima distances of 0.200 and 0.190 nm, respectively. Therefore, the first peak in Figure 7 should be composed of overlapping Li– O^{b} and Li– O^{nb} pairs, and the change in the line shape for the first peak with increasing x corresponds to different Li mole fractions bonding with O^{b} and O^{nb} . In addition, the first peak in the Li– O^{nb} PDF was much narrower than that in Li– O^{b} PDF. The negatively charged O^{nb} can attract Li more strongly than O^{b} because of its stronger Coulombic interactions. The more polarized O^{nb} sites create a

deeper potential at closer Li–O pair positions. The existence of two types of Li bonding with different O types has also been reported with the classical MD simulation,¹⁰ but the mean Li– O^{b} and Li– O^{nb} distances were 0.212 and 0.192 nm, which were inconsistent with our results. The fixed charge of atoms in the classical MD simulation may result in an unrealistic local structure between Li and O^{nb} .

To investigate the charge density distribution, the mean electronic density distribution, $\rho(r)$, surrounding Li was calculated from the snapshots of the first-principles MD simulation. For the spherical electronic configuration, the total electronic number at r was estimated from the $\rho(r)$ of Li. The integrated radial electron number is given by

$$Q(r) = \int \rho_i(r) dv \quad (3)$$

The nuclear charge, $Z_i = 3$, minus $Q(r)$ gives the net atomic charge of Li and is denoted as

$$q(r) = Z_i - Q(r) \quad (4)$$

Figure 9 shows the $Q(r)$ of Li calculated for $x = 0.4$. In this study, we calculated $Q(r)$ for two types of Li, Li^{b} , and Li^{nb} ,

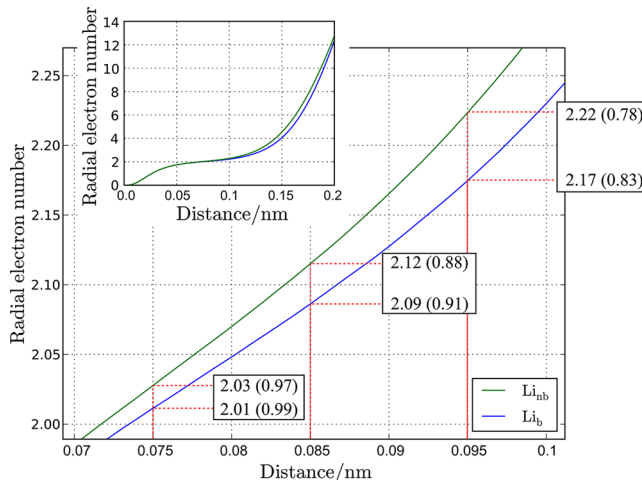


Figure 9. Integrated radial electron numbers of Li for $0.4\text{Li}_2\text{O}-0.6\text{B}_2\text{O}_3$ at 1250 K. The inset figure is the data between 0 and 0.20 nm.

which have neighboring O^{b} and O^{nb} , respectively. The inset in Figure 9 shows the function corresponding to the Li–O distance between 0 and 0.20 nm. A plateau region between 0.070 and 0.10 nm was evident, and the $Q(r)$ and $q(r)$ values at $r = 0.075, 0.085$, and 0.095 nm for Li^{b} and Li^{nb} are shown. The Li^{nb} electron number was greater than that of Li^{b} regardless of the position. This was because negatively charged O^{nb} attracts electrons around Li, forming Coulombic interactions; thus, Li– O^{nb} is more covalent-like than Li– O^{b} . However, more positively charged Li^{b} exists as the naked ion. The Li^{b} and Li^{nb} electron numbers within 0.085 nm corresponding to the first electronic sphere were 2.09 and 2.12, respectively, which are equivalent to net charges of 0.91 and 0.88, respectively. The atomic Mulliken charges for the crystal $\text{Li}_2\text{O}-\text{B}_2\text{O}_3$ system have been reported from theoretical HF-DFT hybrid calculations.³⁵ Mulliken charges obtained with 6-11G(Li), 6-21G*(B), 8-411G*(O) and 7-11G(2d)(Li), 6-21G(2d)(B), 8-411*(O) basis sets were 0.86 and 0.60 for LiBO_2 , giving a composition corresponding to $x = 0.5$. The effective charge in the $\text{Li}_2\text{B}_4\text{O}_7$ crystal calculation from longitudinal optical and

transverse optical splitting in Raman spectroscopy was also reported as 0.8.³⁶ Although Li in the crystal system has a different coordination with O, these net charges are likely to be around 0.8–0.9. Therefore, the decreased net charge of Li obtained from our first-principles MD calculation may reflect the remaining crystal system structure. We calculated D_σ from the conductivity on the basis of the Nernst–Einstein relationship at $q = 1.0$ in Figure 2. We expected that D_σ would be underestimated compared with the real net charge of Li because we used a higher q value. The electron number from the electronic radial distribution function was arbitrary with regard to the cutoff distance, but it is possible to explain the difference between D_{NMR} and D_σ .

The mean square displacements (MSDs) of Li as a function of time were evaluated from the atomic configuration. Figure 10

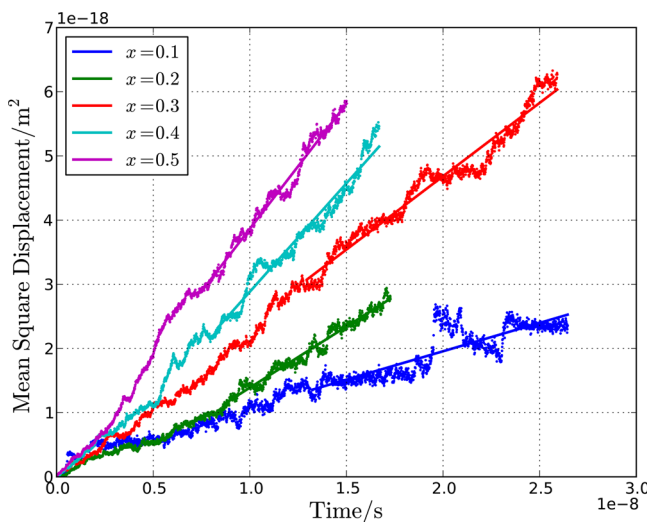


Figure 10. Mean-square displacements of Li in a molten $x\text{Li}_2\text{O}-(1-x)\text{B}_2\text{O}_3$ system at 1250 K. The lines are linear regressions used to calculate the Li self-diffusion coefficient.

shows the MSDs of Li in the $x\text{Li}_2\text{O}-(1-x)\text{B}_2\text{O}_3$ system at 1250 K and the linear regression lines used to obtain the Li self-diffusion coefficient on the basis of the Einstein relationship. The lines were obtained for the last 10 ps of the simulation period. The calculated Li self-diffusion coefficients are plotted with the experimental and classical MD results in Figure 11, as a function of the composition. The classical MD results show a clear discrepancy for the system at $x = 0.5$. Neglect of polarizability and charge transfer through using a fixed charge model leads to reduced dynamics at higher Li contents. However, although there was a consistent difference between the experimental and first-principles MD results between $x = 0.2$ and 0.5, the trends were in good agreement with experimental data and were able to reproduce Li transport in the glass melts.

CONCLUSIONS

We have presented experimental results of conductivity measurements and a comparison with Li self-diffusion coefficients obtained from NMR measurements. The D_σ/D_{NMR} ratios were 2.5–3.2 at 1250 K. First-principles MD simulations of the same $x\text{Li}_2\text{O}-(1-x)\text{B}_2\text{O}_3$ system were carried out to determine the atomic and electronic structures. The structural features of the B–O networks were studied in terms of B–O, Li–O PDFs, $\text{BO}_4/(\text{BO}_4 + \text{BO}_3)$ values, and O–

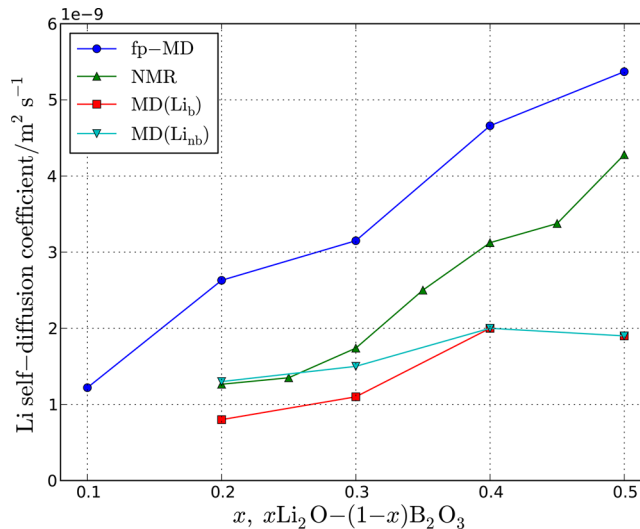


Figure 11. Li self-diffusion coefficients as a function of composition in $x\text{Li}_2\text{O}-(1-x)\text{B}_2\text{O}_3$ at 1250 K. A comparison is made with MD(Li^b) bonding with bridging O and MD(Li^{nb}) bonding with non-bridging oxygen obtained from classical MD simulation¹⁰ and experimental NMR results.¹¹

B–O angle distribution functions. The O–B–O angle distribution functions showed a broadened peak at approximately 120° regardless of composition. We believe that the B–O network structure is composed of strongly disordered BO_4^- and BO_3 units. The mean Li–O distance was slightly dependent on composition, because of the contributions of the molar ratios of two types of Li, coordinated to O^b and O^{nb} in the glass network. The Li electronic structure was analyzed to obtain the electronic radial distribution function. Although the electron number from the electronic radial distribution function was arbitrary with regard to the cutoff distance, the electron numbers integrated within 0.085 nm were 2.12 and 2.09, corresponding to net charges of 0.88 and 0.91, for Li^{nb} and Li^b , respectively, and they followed a similar decreasing trend in Raman spectroscopy and HF-DFT hybrid calculations in the crystal system. This suggests that D_{NMR}/D_σ can be described by the decrease in Li net charge. Li self-diffusion coefficients were evaluated from the atomic configuration, and our first-principles MD results for compositions with higher Li content agreed better with the experimental data than did the classical MD results, which did not include the possibility of ionic polarizability. We conclude that the atomic and electronic structures obtained from first-principles MD simulation offer a good understanding of experimentally observed electronic properties.

ASSOCIATED CONTENT

Web-Enhanced Feature

A video of Li moving back and forth within a cavity for a period of 1 ps is available in the HTML version of the paper.

AUTHOR INFORMATION

Corresponding Author

*E-mail: ohkubo.takahiro@faculty.chiba-u.jp. Phone: +81 (0) 43 2903435. Fax: +81 (0)43 2903431.

Notes

The authors declare no competing financial interest.

ACKNOWLEDGMENTS

The computation was mainly performed using the computer facilities at the Research Institute for Information Technology, Kyushu University.

REFERENCES

- (1) Matsuo, T.; Shibusaki, M.; Katsumata, T. Diffusion of Li Ion in Glassy $\text{Li}_2\text{O}-\text{B}_2\text{O}_3$ System. *Solid State Ionics* **2002**, *154*, 759–766.
- (2) Matsuo, T.; Yagami, T.; Katsumata, T. Electric Conduction of Single Crystal and Glass of $\text{Li}_2\text{B}_4\text{O}_7$. *J. Appl. Phys.* **1993**, *74*, 7264–7268.
- (3) Ito, Y.; Miyauchi, K.; Oi, T. Ionic Conductivity of $\text{Li}_2\text{O}-\text{B}_2\text{O}_3$ Thin Films. *J. Non-Cryst. Solids* **1983**, *57*, 389–400.
- (4) Yano, T.; Kunimine, N.; Shibata, S.; Yamane, M. Structural Investigation of Sodium Borate Glasses and Melts by Raman Spectroscopy. II. Conversion between BO_4 and BO_2O^- Units at High Temperature. *J. Non-Cryst. Solids* **2003**, *321*, 147–156.
- (5) Zhong, J.; Bray, P. Change in Boron Coordination in Alkali Borate Glasses, and Mixed Alkali Effects, as Elucidated by NMR. *J. Non-Cryst. Solids* **1989**, *111*, 67–76.
- (6) Feller, S.; Dell, W.; Bray, P. ^{10}B NMR Studies of Lithium Borate Glasses. *J. Non-Cryst. Solids* **1982**, *51*, 21–30.
- (7) Sen, S. Temperature Induced Structural Changes and Transport Mechanisms in Borate, Borosilicate and Boroaluminate Liquids: High-Resolution and High-temperature NMR Results. *J. Cryst. Growth* **1999**, *253*, 84–94.
- (8) Stebbins, J.; Ellsworth, S. Temperature Effects on Structure and Dynamics in Borate and Borosilicate Liquids: High-resolution and High-Temperature NMR Results. *J. Am. Ceram. Soc.* **1996**, *79*, 2247–2256.
- (9) Verhoef, A.; Den Hartog, H. Structure and Dynamics of Alkali Borate Glasses: a Molecular Dynamics Study. *J. Non-Cryst. Solids* **1995**, *182*, 235–247.
- (10) Varsamis, C.; Vegiri, A.; Kamitsos, E. Molecular Dynamics Investigation of Lithium Borate Glasses: Local Structure and Ion Dynamics. *Phys. Rev. B* **2002**, *65*, 104203–104217.
- (11) Ohkubo, T.; Gobet, M.; Sarou-Kanian, V.; Bessada, C.; Nozawa, M.; Iwadate, Y. Self-Diffusion Coefficient of Lithium in Molten $x\text{Li}_2\text{O}-(1-x)\text{B}_2\text{O}_3$ System Using High-Temperature PFG NMR. *Chem. Phys. Lett.* **2012**, *530*, 61–63.
- (12) Iwadate, Y.; Igarashi, K.; Mochinaga, J. Electrical Conductivity of Molten Charge-asymmetric Salts $\text{PrCl}_3-\text{NaCl}$, PrCl_3-KCl , and $\text{PrCl}_3-\text{CaCl}_2$ Systems. *J. Electrochem. Soc.* **1986**, *133*, 1162–1166.
- (13) Janz, G. Molten Salts Data as Reference Standards for Density, Surface Tension, Viscosity, and Electrical Conductance: KNO_3 and NaCl ; American Chemical Society and the American Institute of Physics for the National Bureau of Standards, 1981.
- (14) Shi, X.; Wang, Q.; Li, C.; Niu, X.; Wang, F.; Lu, K. Densities of $\text{Li}_2\text{O}-\text{B}_2\text{O}_3$ Melts. *J. Cryst. Growth* **2006**, *290*, 637–641.
- (15) Kohn, W.; Sham, L. Self-Consistent Equations Including Exchange and Correlation Effects. *Phys. Rev.* **1965**, *140*, A1133–A1138.
- (16) Tsuchida, E.; Tsukada, M. Large-Scale Electronic-Structure Calculations Based on the Adaptive Finite-Element Method. *J. Phys. Soc. Jpn.* **1998**, *67*, 3844–3858.
- (17) Tsuchida, E.; Tsukada, M. Adaptive Finite-Element Method for Electronic-Structure Calculations. *Phys. Rev. B* **1996**, *54*, 7602–7605.
- (18) Berendsen, H.; Postma, J.; Van Gunsteren, W.; DiNola, A.; Haak, J. Molecular Dynamics with Coupling to an External Bath. *J. Chem. Phys.* **1984**, *81*, 3684–3690.
- (19) Tsuchida, E. Ab Initio Molecular-Dynamics Study of Liquid Formamide. *J. Chem. Phys.* **2004**, *121*, 4740–4746.
- (20) Rollet, A.; Sarou-Kanian, V.; Bessada, C. Measuring Self-Diffusion Coefficients up to 1500 K: A Powerful Tool to Investigate the Dynamics and the Local Structure of Inorganic Melts. *Inorg. Chem.* **2009**, *48*, 10972–10975.
- (21) Murch, G. The Haven Ratio in Fast Ionic Conductors. *Solid State Ionics* **1982**, *7*, 177–198.
- (22) Thomas, M.; Peterson, N. Electrical Conductivity and Tracer Diffusion in Sodium Germanate Glasses. *Solid State Ionics* **1984**, *14*, 297–307.
- (23) Kaps, C.; Schirrmeister, F.; Stefanski, P. On the Na^+ Self-Diffusion and Electrical Conductivity of $\text{Na}_2\text{O}-\text{B}_2\text{O}_3-\text{SiO}_2$ Glasses Derived from the $\text{Na}_2\text{O}-\text{SiO}_2$ Glass. *J. Non-Cryst. Solids* **1986**, *87*, 159–170.
- (24) Tokuda, H.; Tsuzuki, S.; Susan, M.; Hayamizu, K.; Watanabe, M. How Ionic Are Room-Temperature Ionic Liquids? An Indicator of the Physicochemical Properties. *J. Phys. Chem. B* **2006**, *110*, 19593–19600.
- (25) Noda, A.; Hayamizu, K.; Watanabe, M. Pulsed-Gradient Spin-Echo ^1H and ^{19}F NMR Ionic Diffusion Coefficient, Viscosity, and Ionic Conductivity of Non-Chloroaluminate Room-Temperature Ionic Liquids. *J. Phys. Chem. B* **2001**, *105*, 4603–4610.
- (26) Humphrey, W.; Dalke, A.; Schulten, K. VMD: Visual Molecular Dynamics. *J. Mol. Graphics* **1996**, *14*, 33–38.
- (27) Zhigadlo, N. Unusual Behaviour of Lithium Tetraborate $\text{Li}_2\text{B}_4\text{O}_7$ at Low Temperatures: An X-ray Diffraction Study. *Phys. Status Solidi* **1995**, *152*, 329–339.
- (28) Markgraf, S.; Furukawa, Y.; Sato, M.; Bhalla, A. Pyroelectric, Dielectric, and Piezoelectric Properties of LiB_3O_5 . *J. Appl. Phys.* **1995**, *78*, 7234–7239.
- (29) Jiang, A.; Lei, S.; Huang, Q.; Chen, T.; Ke, D. Structure of Lithium Heptaborate, $\text{Li}_3\text{B}_7\text{O}_{12}$. *Acta Crystallogr., Sect. C* **1990**, *46*, 1999–2001.
- (30) Swenson, J.; Börjesson, L.; Howells, W. Structure of Fast-Ion-Conducting Lithium and Sodium Borate Glasses by Neutron Diffraction and Reverse Monte Carlo Simulations. *Phys. Rev. B* **1998**, *57*, 13514–13526.
- (31) Shibata, M.; Sanchez, C.; Patel, H.; Feller, S.; Stark, J.; Sumcad, G.; Kasper, J. The Density of Lithium Borate Glasses Related to Atomic Arrangements. *J. Non-Cryst. Solids* **1986**, *85*, 29–41.
- (32) Dell, W.; Bray, P. ^{11}B NMR Studies and Structural Modeling of $\text{Na}_2\text{O}-\text{B}_2\text{O}_3-\text{SiO}_2$ Glasses of High Soda Content. *J. Non-Cryst. Solids* **1983**, *58*, 1–16.
- (33) Kirfel, A.; Will, G.; Stewart, R. The Chemical Bonding in Lithium Metaborate, LiBO_2 . Charge Densities and Electrostatic Properties. *Acta Crystallogr., Sect. B* **1983**, *39*, 175–185.
- (34) Bondareva, O.; Egorov, T.; Simonov, M.; Malinovskii, Y.; N. V. B. Sov. Phys. Crystallogr. **1980**, *25*, 313–318.
- (35) Maslyuk, V.; Islam, M.; Bredow, T. Electronic Properties of Compounds of the $\text{Li}_2\text{O}-\text{B}_2\text{O}_3\text{O}$ System. *Phys. Rev. B* **2005**, *72*, 125101–125109.
- (36) Vdovin, A.; Moiseenko, V.; Gorelik, V.; Burak, Y. Vibrational Spectrum of $\text{Li}_2\text{B}_4\text{O}_7$ Crystals. *Phys. Solid State* **2001**, *43*, 1648–1654.